Measuring the EoR Power Spectrum Without Measuring the EoR Power Spectrum

Angus Beane, 1, 2 Francisco Villaescusa-Navarro, 1 and Adam Lidz²

¹ Center for Computational Astrophysics, Flatiron Institute, 162 5th Ave., New York, NY 10010, USA
² Department of Physics & Astronomy, University of Pennsylvania, 209 South 33rd St., Philadelphia, PA 19104, USA

Submitted to ApJ

ABSTRACT

The large-scale structure of the Universe should soon be measured at high redshift during the Epoch of Reionization (EoR) through line-intensity mapping. A number of ongoing and planned surveys are using the 21 cm line to trace neutral hydrogen fluctuations in the intergalactic medium (IGM) during the EoR. These may be fruitfully combined with separate efforts to measure large-scale emission fluctuations from galactic lines such as [C II], CO, H- α , and Ly- α during the same epoch. The large scale power spectrum of each line encodes important information about reionization, with the 21 cm power spectrum providing a relatively direct tracer of the ionization history. Here we show that the large scale 21 cm power spectrum can be extracted using only cross-power spectra between the 21 cm fluctuations and each of two separate line-intensity mapping data cubes. This technique is more robust to residual foregrounds than the usual 21 cm auto-power spectrum measurements and so can help in verifying auto-spectrum detections. We characterize the accuracy of this method using numerical simulations and find that the large-scale 21 cm power spectrum can be inferred to a simulated accuracy of within 5% for most of the EoR. Our estimate of the 21 cm power spectrum reaches 0.6% accuracy on a scale of $k \sim 0.1 \,\mathrm{Mpc^{-1}}$ at $\langle x_i \rangle = 0.36$ (z = 8.34 in our model). An extension from two to N additional lines would provide N(N-1)/2 cross-checks on the large-scale 21 cm power spectrum. This work strongly motivates redundant line-intensity mapping surveys probing the same cosmological volumes.

Keywords: large-scale structure of universe — cosmology: theory — dark ages, reionization, first stars — diffuse radiation

1. INTRODUCTION

Upcoming 21 cm surveys are poised to make a first detection of redshifted 21 cm fluctuations from the EoR within the next several years (DeBoer et al. 2017). These measurements will provide a direct probe of the distribution of neutral hydrogen in the IGM, revealing the spatial structure of the reionization process, and its redshift evolution. Along with these measurements, several other "line-intensity" mapping surveys are planned to map out large-scale structure in the galaxy distribution using convenient emission lines with current targets including [C II], CO, Ly- α , and H- α (see e.g. Kovetz et al. 2017, and references therein). These surveys study the spatial fluctuations in the collective emission from

Corresponding author: Angus Beane abeane@sas.upenn.edu

many individually unresolved sources (e.g. Suginohara et al. 1999; Righi et al. 2008; Visbal & Loeb 2010). These measurements should nicely complement 21 cm observations (e.g. Lidz et al. 2011; Gong et al. 2011): while the 21 cm fluctuations trace-out remaining neutral hydrogen residing mostly in the low-density IGM, the galactic emission lines track the galaxies themselves, which presumably lie within "bubbles" of mostly ionized hydrogen (Lidz et al. 2009).

In fact, recent work has led to detections in various lines at low redshift (Chang et al. 2010; Davis et al. 2001; Keating et al. 2016; Pullen et al. 2018; Croft et al. 2016; Croft et al. 2018), bolstering efforts to employ the line-intensity mapping technique at earlier times during the EoR. It is hence timely to explore the scientific benefits of combining 21 cm observations of the EoR with line-intensity mapping surveys in other emission lines.

Here we consider, for the first time, one potential advantage of combining 21 cm surveys of the EoR with line-intensity mapping surveys in two additional lines. Specifically, we show that the linear bias factor of the 21 cm field may be extracted solely from cross-power spectra between the 21 cm fluctuations and those in each of two separate lines. This can provide an important cross-check on inferences from the 21 cm autopower spectrum since cross-power spectra should be less prone to bias from residual foregrounds (e.g. Furlanetto & Lidz 2007; Lidz et al. 2009); only shared foregrounds contribute to the average cross spectrum signal.

The foreground problem is especially daunting in the case of redshifted 21 cm surveys, where the expected foreground-to-signal strength is on the order of $\sim 10^5$ (e.g. Bernardi et al. 2009; Pober et al. 2013; Dillon et al. 2014). The basic strategy for extracting the signal is to exploit the fact that the foregrounds should be smooth functions of frequency, while the reionization signal has a great deal of spectral structure. In practice, this is challenging because the instrument, calibration errors, and other effects may imprint artificial spectral variations. Cross-spectrum measurements should be less sensitive to such systematic effects and can therefore help confirm early detections. For instance, Villaescusa-Navarro et al. (2015) show that cross-spectra can be robustly measured even in the presence of polarized synchrotron foregrounds; this is a troublesome case for auto-spectrum analyses because Faraday rotation leads to frequency structure.

The amplitude of the 21 cm power spectrum evolves with redshift in a distinctive way as reionization proceeds (e.g. Lidz et al. 2008), and recent work has demonstrated that linear biasing describes the large-scale 21 cm power spectrum rather well (McQuinn & D'Aloisio 2018; Hoffmann et al. 2018; Beane & Lidz 2018). Therefore, if our three-field method may be employed over a range of redshifts, it can be used to extract key and robust information regarding the reionization history of the Universe.

In recent related work we showed that the large-scale 21 cm bias factor may be recovered using suitable cross-bispectra between the 21 cm fluctuations and the [C II] emission field (Beane & Lidz 2018). While the cross-bispectra method requires only the 21 cm fluctuations and one additional tracer field, the technique we propose here should be vastly simpler to implement in practice (provided two additional tracers are available with common sky and redshift coverage). This is the case because our present method relies only on two-point statistics, and it therefore avoids practical difficulties in carrying out cross-bispectrum analyses. For example, it is chal-

lenging to estimate the bispectrum covariance as this involves computing a six-point function. In addition, we will show that our present technique allows for a more faithful extraction of the 21 cm bias factor. Ultimately, both analyses may be carried out for additional cross-checks.

There are a broad range of possible lines that may be combined with the 21 cm surveys. Currently, there are projects - either ramping-up or in the planning stages – to perform EoR-era line-intensity surveys in: [C II] $158 \,\mu\mathrm{m}$ (Crites et al. 2014; Lagache 2017; Vavagiakis et al. 2018), rotational transitions from CO molecules (Chung et al. 2017), Ly- α (Doré et al. 2016), and H- α (Cooray et al. 2016). Additional fine-structure lines such as $[O III] 88 \mu m$ (Moriwaki et al. 2018) and [N II] $122 \,\mu\mathrm{m}$ (Serra et al. 2016) may also be suitable — in some cases, these lines will land in the proposed frequency bands of the planned [C II] surveys. The [O III] 88 µm line appears especially promising since targeted ALMA observations around $z \sim 7-9$ galaxies have found that this line is brighter at high redshift than expected based on local correlations between lineluminosity and star-formation rate (e.g. Moriwaki et al. 2018, and references therein).

In principle, one could extract the 21 cm bias using the cross-spectrum with a traditional galaxy survey, in which case the galaxy bias may be measured robustly from the auto-power spectrum. In practice, this is extremely challenging because one needs spectroscopic redshifts for the galaxy survey over a huge sky area at $z\sim 8$. If only photometric redshifts are available, then one only accesses long-wavelength line-of-sight modes (with small or vanishing line-of-sight wavenumbers) in the galaxy survey but precisely these modes are lost to foreground cleaning/avoidance in the 21 cm surveys (e.g. Lidz et al. 2009). Fortunately, multi-line intensity mapping provides a promising way forward here and our approach avoids measuring bias factors from auto-spectra.

In Section 2, we describe our three cross-spectra approach in detail. In Section 3 we briefly discuss the radiative transfer simulations of reionization (McQuinn et al. 2007; Lidz et al. 2008) used in our analysis, the reionization model assumed, and our method for generating mock line-intensity mapping data cubes. We then quantify the accuracy of our technique in Section 4. The survey specifications required to extract bias factors with this method are discussed briefly in Section 5. We conclude in Section 6. We assume a Λ CDM cosmology, parameterized by $(\Omega_m, \Omega_\Lambda, \Omega_b, h, \sigma_8, n_s) = (0.27, 0.73, 0.046, 0.7, 0.8, 1)$ as in the simulations used in this work (McQuinn et al. 2007). While these parameters differ slightly from presently favored values (e.g.

Planck Collaboration et al. 2018), this should not impact our conclusions.

2. APPROACH

Here we define terms and describe our three crossspectra approach. Ignoring redshift-space distortions and spin-temperature fluctuations, the 21 cm brightness temperature contrast between neutral hydrogen gas and the cosmic microwave background is:

$$T_{21}(\boldsymbol{x}) = T_0 X_{\text{HI}}(\boldsymbol{x}) [1 + \delta_{\rho}(\boldsymbol{x})]. \tag{1}$$

Here $T_0 = 28 \,\mathrm{mK}[(1+z)/10]^{1/2}$ (e.g. Zaldarriaga et al. 2004), $X_{\rm HI}(\boldsymbol{x})$ is the neutral hydrogen fraction at position \boldsymbol{x} , and $\delta_{\rho}(\boldsymbol{x})$ is the gas density contrast, which is assumed to follow the overall matter density field on the large scales of interest. Although ionized regions imprint large-scale fluctuations in the 21 cm field, on scales much larger than the size of the ionized regions, the 21 cm fluctuations should nevertheless follow a linear biasing relation

$$T_{21}(\mathbf{k}) = \pm \langle T_{21} \rangle b_{21} \delta_{\text{lin}}(\mathbf{k}), \tag{2}$$

where the \pm indicates that the fields are either correlated (+) or anti-correlated (-) — during the bulk of the EoR, the 21 cm and density fields are anti-correlated on large scales in most models (e.g. Lidz et al. 2009). Here $T_{21}(\mathbf{k})$ is the Fourier transform of the brightness temperature field (Equation 1) and $\delta_{\text{lin}}(\mathbf{k})$ is the Fourier transform of the linear density contrast. The quantity b_{21} is the dimensionless, and scale-independent, linear bias factor of the 21 cm fluctuation contrast, $\delta_{21}(\mathbf{x}) = (T_{21}(\mathbf{x}) - \langle T_{21} \rangle) / \langle T_{21} \rangle$, while the $\langle T_{21} \rangle$ factor reverts to brightness temperature units (since the average brightness temperature is not itself observable from interferometric measurements.) In this work when we refer to the "bias" we mean $\langle T_{21} \rangle b_{21}$ (and likewise for the intensity mapping surveys.)

Likewise, we can consider additional tracer lines, such as [C II]. On large scales, the Fourier transform of the specific intensity of each of these lines should be well-described by

$$I_i(\mathbf{k}) = \langle I_i \rangle b_i \delta_{\text{lin}}(\mathbf{k}),$$
 (3)

where $\langle I_i \rangle$ is the mean specific intensity of the emission line.² For the case of emission lines sourced by

gas within galaxies, the relevant bias factor is the luminosity-weighted bias of the line-emitting host halos (e.g. Lidz et al. 2011). To be completely general we should also include a \pm here (as in Equation 2), but for the galactic emission lines we generally expect brighter line emission in overdense regions.

On sufficiently large scales, the auto-power spectrum of the fluctuations in each tracer line (Equation 3) will be

$$P_{i,i}(k,z) \equiv \langle I_i(k,z)I_i^*(k,z)\rangle$$

= $[\langle I_i\rangle(z)b_i(z)]^2 P_{\text{lin}}(k,z),$ (4)

where $P_{\text{lin}}(k,z)$ is the linear matter power spectrum. Similarly, on large scales the 21 cm auto-power spectrum should follow $P_{21,21}(k,z) = \left[\langle T_{21} \rangle (z) b_{21}(z) \right]^2 P_{\text{lin}}(k,z)$. In principle, one can infer the bias factors $\langle I_i \rangle b_i$ and $\langle T_{21} \rangle b_{21}$ from auto-power spectrum measurements (assuming a model for the linear power spectrum). However, foreground cleaning/avoidance present significant challenges here (e.g. Liu & Tegmark 2012; Moore et al. 2013; Thyagarajan et al. 2015; Pober et al. 2016; Ewall-Wice et al. 2017) and residual foregrounds may bias such inferences.

Another approach is to measure the cross-power spectrum between two lines i and j. In this case, one measures

$$P_{i,j} = r_{i,j} \langle I_i \rangle \langle I_j \rangle b_i b_j P_{\text{lin}}, \tag{5}$$

where $r_{i,j}$ is the cross-correlation coefficient which ranges from -1 to $1.^3$ In the above equation and in what follows, we generally suppress redshift and wavenumber labels for brevity. In general, $r_{i,j}$ is scale-dependent, but asymptotes to -1 (for anticorrelated fields) or 1 (for correlated fields) on large scales.⁴ If one of the lines is the 21 cm field, we replace $\langle I_i \rangle$ with $\langle T_{21} \rangle$ in Equation 5.

However, in the presence of a third line k, and with $P_{j,k}$ and $P_{k,i}$ defined analogously as in Equation 5, we

¹ Our Fourier convention is: $T_{21}(\mathbf{k}) = \int d^3x \, T_{21}(\mathbf{x}) e^{i\mathbf{k}\cdot\mathbf{x}}$ and $T_{21}(\mathbf{x}) = \int \frac{d^3k}{(2\pi)^3} \, T_{21}(\mathbf{k}) e^{-i\mathbf{k}\cdot\mathbf{x}}$.

² We follow standard conventions in expressing 21 cm fluctuations in brightness temperature units, i.e. in mK, while we use specific intensity units for the other tracer lines, i.e. I_i is the specific intensity in Jy/str.

³ Note that here we adopt the convention that the bias factors are always positive and that the sign of the cross-spectrum is determined solely by that of the correlation coefficient. This convention differs from our previous work (Beane & Lidz 2018).

⁴ Note that we neglect shot-noise contributions to the auto-spectrum in Equation 4, as well as correlated shot-noise terms in the cross-power spectrum. This should be a very good approximation on the scales of interest unless the line-emitting sources are quite rare (e.g. Lidz & Taylor 2016). Even in the case of rare sources, the shot-noise term should be a white-noise contribution on scales much larger than the size of the host halos. In this case, one can perform a joint fit for the shot-noise along with the clustering terms.

can simply write

$$P_{i,i} = (\langle I_i \rangle b_i)^2 P_{\text{lin}} = \frac{r_{j,k}}{r_{i,j} r_{k,i}} \frac{P_{i,j} P_{k,i}}{P_{j,k}}$$

$$\equiv R_{i,j,k} P_{i,j,k},$$
(6)

where we have defined $R_{i,j,k} \equiv r_{j,k}/(r_{i,j}r_{k,i})$ and $P_{i,j,k} \equiv (P_{i,j}P_{k,i})/P_{j,k}$. On sufficiently large scales, $R_{i,j,k} \rightarrow 1$, but on intermediate scales $R_{i,j,k} > 1$ for most reasonable cases when the various r's are close in magnitude. Equation 6 shows that (on sufficiently large scales where linear biasing holds and $R_{i,i,k} \sim 1$) we can recover the linear bias factor of field i from a suitable ratio of cross-spectra. Here we suppose that the underlying density power spectrum is well known. Equation 6 is the main point of this paper; in the remainder of this work we consider an application to the EoR and quantify its accuracy. Specifically, we will test the range of validity – in spatial scale and redshift/ionization fraction – of the assumption that $R_{i,j,k} = 1$, along with the linear biasing approximations of Equations 2 & 3. Note that testing the assumption that $R_{i,j,k} = 1$ directly from upcoming data will require reliable auto-spectra.

We turn now to the specific case of EoR surveys with the goal of extracting the 21 cm bias factor using only cross-power spectra. For further specificity we suppose that the two additional tracer lines are [C II] and [O III], although little of the analysis that follows depends on the choice of these two lines — any of the lines mentioned in Section 1 can be used instead of [C II] or [O III]. In this case, Equation 6 may be applied as

$$P_{21,21} = (\langle T_{21} \rangle b_{21})^2 P_{\text{lin}}$$

$$= \frac{P_{21,\text{C II}} P_{\text{O III},21}}{P_{\text{C II,O III}}},$$
(7)

i.e. assuming $R_{21,C \text{ II},O \text{ III}} = 1$.

We expect this approach to break down on small scales. First, the three fields will be well-correlated (or anti-correlated) only on large scales, with the 21 cm field and the [C II], [O III] fields decorrelating on scales smaller than the size of the ionized regions (Lidz et al. 2011). Second, we assume linear biasing which should break down on scales where second-order bias terms become significant (McQuinn & D'Aloisio 2018).

One caveat here is that we neglect redshift space distortions throughout. Including these effects will make the power spectra in Equation 7 angle-dependent. Although these effects are well studied in the case of the 21 cm auto-spectrum (e.g. Mao et al. 2012), an extension of our three cross-spectra method may be needed to account for these distortions.

3. SIMULATIONS

In order to investigate the accuracy of Equation 7 we turn to $(186\,\mathrm{Mpc})^3$ radiative transfer simulations of the EoR (McQuinn et al. 2007; McQuinn et al. 2007; Lidz et al. 2008). In these calculations, radiative transfer is post-processed onto a $(1024)^3$ dark matter only simulation run with GADGET-2 (Springel 2005). The dark matter simulation resolves halos only down to $10^{10}\,\mathrm{M}_\odot$, however halos down to $10^8\,\mathrm{M}_\odot$ are added manually in post-processing with the correct statistical properties (McQuinn et al. 2007). Halos resolved directly in the simulation (i.e. $> 10^{10}\,\mathrm{M}_\odot$) are identified with a Friends-of-Friends algorithm with a linking length of 0.2.

In what follows, we adopt the abundant mini-halo sink scenario (McQuinn et al. 2007; Lidz et al. 2008) as our baseline reionization model. Although the detailed model for photon sinks implemented in these simulations may not be fully realistic, the smaller ionized regions in "abundant sink" scenarios may, in fact, be more plausible than the other cases considered in this previous work (McQuinn & D'Aloisio 2018). In any case, the accuracy of our method does not depend strongly on the precise reionization model assumed.

In order to model the [C II] and [O III] emission fluctuations, we assume that the luminosity in each line is correlated with the host halo mass. Specifically, we adopt a power-law average relation between line-luminosity and halo mass:

$$\langle L_i \rangle(M) = L_{i,0} \left[\frac{M}{M_0} \right]^{\alpha_i},$$
 (8)

where M is the mass of the halo, $\langle L_i \rangle$ is the average luminosity, and $L_{i,0}$ is the luminosity at characteristic mass M_0 . In order to account for scatter in this relation, we add a random number so that each halo's luminosity is $L_i = \langle L_i \rangle (1 + \epsilon)$ where ϵ is drawn from a zero-mean lognormal distribution of width 0.4 dex.

In what follows we assume that each host halo in the simulation hosts a [C II] and [O III] emitter. If only a random fraction f of halos host active [C II] and/or [O III] emitters while $L_{i,0}$ is boosted to fix the average specific-intensity in each line, this does not change the 21 cm-[C II] or 21 cm-[O III] cross-power spectra. This represents the case that star-formation activity has a short duty-cycle, yet the total star-formation rate density is fixed to the observed value. If the same random fraction emit in both [C II] and [O III] this can boost the cross-shot noise contribution to $P_{\rm C II,O III}$, but this is highly sub-dominant on the scales of interest ($k \leq 0.4$ Mpc⁻¹) even for $f = 10^{-2}$.

In order to estimate the specific intensity of the two fields, we use nearest grid-point interpolation to estimate the emissivity on a 512^3 Cartesian grid, matching

the resolution of the density and 21 cm fields from Lidz et al. (2008). Note that we can test the accuracy of Equation 7 without specifying the numerical value of $L_{i,0}$ or M_0 since they cancel in the ratio. The value of α_i , on the other hand, controls which host-halos (and galactic star-formation rates) produce most of the specific intensity in line i.⁵ If the value of α_i is the same for [C II] and [O III], then the two fields differ only by an overall multiplicative factor and Equation 7 reduces to a simple ratio between a single cross-spectrum and an auto-spectrum.⁶

We consider three different values for α_i : 2/3, 1, and 4/3. We refer to these as L, M, and H since they provide most weight to low, medium, and high mass host-halos respectively. We allow for the case that the two lines have different values of α_i : i.e., we consider 21 cm-L-M, 21 cm-M-H, and 21 cm-H-L, with L, M, or H standing in for [C II] or [O III] in Equation 7. We then measure the various cross-spectra using a slightly modified version of the power spectrum calculator in 21cmFAST (Mesinger et al. 2011; Park et al. 2018).

4. RESULTS

We first investigate how well our three cross-spectra approach for measuring the large-scale 21 cm bias agrees with the true bias. We measure the true bias as

$$\langle T_{21} \rangle b_{21}(k) \equiv \sqrt{\frac{P_{21,21}(k)}{P_{\delta,\delta}(k)}},$$
 (9)

and also estimate the bias as

$$\langle T_{21} \rangle b_{21}(k) \simeq \left| \frac{P_{21,\delta}(k)}{P_{\delta,\delta}(k)} \right|,$$
 (10)

where $P_{\delta,\delta}(k)$ is the auto-power spectrum of the simulated density field and $P_{21,\delta}(k)$ is the 21 cm-density cross-power spectrum. Note that Equation 10 assumes that the correlation coefficient $|r_{21,\delta}| = 1$ and so will depart from Equation 9 on small scales, but the two should converge on large scales (see Section 1). The absolute value in Equation 10 comes about from the

convention adopted in Section 2. On large scales where the 21 cm, [C II], and [O III] fields are each well correlated or anti-correlated with the density field and linear theory applies, we expect all estimates of $\langle T_{21} \rangle b_{21}$ to agree. When we estimate the bias factors using our three cross-spectra method (Equation 7) we use the simulated density power-spectrum, since this is extremely close to the linear theory prediction on the relevant scales and redshifts.

The bias factors inferred from Equation 7 are shown in Figure 1 for each of the three combinations of our luminosity-mass relation models (L-M, M-H, H-L) at z = 8.34 when the model volume-averaged ionization fraction is $\langle x_i \rangle = 0.36$. These are compared with the bias inferred from the 21 cm auto-spectrum (Equation 9) and the 21 cm-density cross-spectrum (Equation 10). On large scales $(k \lesssim 0.3 \,\mathrm{Mpc}^{-1})$, the methods converge to very nearly the same value. We find that on a scale of $k = 0.1 \,\mathrm{Mpc}^{-1}$ at $\langle x_i \rangle = 0.36$ the three methods agree with the true value to within 0.6%. In the case of 21 cm-L-L, 21 cm-M-M, or 21 cm-H-H models the agreement is slightly worse but still at the percent-level. Note that another approach for estimating the 21 cm bias would use only the 21 cm-[C II] cross-spectrum and the [C II] auto-spectrum. This requires measuring the [C II] auto-spectrum, which is subject to contamination from interloping line emission, and so we pursue only the more robust three-field technique here.

The success results because the ionized regions are sufficiently smaller than this scale ($k=0.1\,\mathrm{Mpc}^{-1}$), ensuring that the 21 cm and line-intensity fields are highly anti-correlated and that second-order biasing contributions are small. For example, the cross-correlation coefficient between the 21 cm field and the density field is $r_{21,\delta}=-0.99$ at $k=0.1\,\mathrm{Mpc}^{-1}$ for $\langle x_i\rangle=0.36,$ z=8.34.

On smaller scales, our approach breaks down. At $\langle x_i \rangle = 0.36$, the different bias factor estimates begin diverging at the $\geq 10\%$ level near $k \sim 0.4\,\mathrm{Mpc}^{-1}$. This occurs because the fields start to de-correlate and second order biasing terms become more important. As anticipated after Equation 6, the three cross-spectra approach underestimates the bias factor in this regime. This underestimation may allow one to place robust lower limits on $P_{21,21}$ that are only $\sim 50\%$ smaller than the true value down to $k \sim 2\,\mathrm{Mpc}^{-1}$ at this stage of the EoR, although the model-dependence of such limits warrants further investigation.

At later times, the average ionization fraction and the bubble sizes increase and so the scale at which the linear biasing approximation breaks down moves to larger scales. For example, at $\langle x_i \rangle = 0.7$ (z = 7.32),

 $^{^5}$ Note we assume that the minimum host halo mass of the [C II] and [O III] emitters is $10^8 M_{\odot}$, comparable to the atomic cooling mass. The true minimum host mass of the emitters may, in fact, be larger. However, note that the average specific intensity may be fixed by the total star-formation rate density and the line-luminosity star-formation rate correlation. Provided these quantities are fixed, then the main impact of boosting the minimum host halo mass will be to increase slightly the bias factors, b_i , and the signal strength. See e.g. (Lidz & Taylor 2016) for more details regarding line-intensity fluctuation models.

 $^{^6}$ This assumes, as we do here, that the scatter in the luminosity-mass relation is perfectly correlated between [C II] and [O III] at fixed $\alpha_i.$

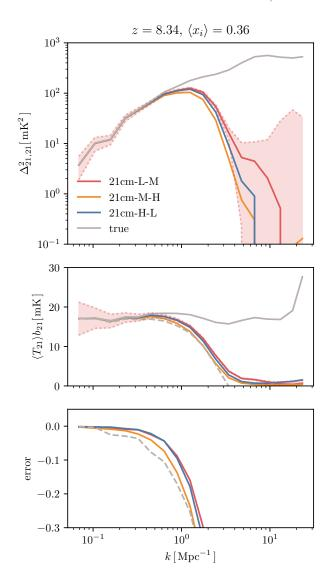


Figure 1. Upper: The simulated, dimensionless 21 cm auto-power spectrum (gray) compared to that inferred from our three-cross spectra approach assuming linear biasing at $\langle x_i \rangle = 0.36, z = 8.34$. The different colors correspond to various possible line-luminosity mass relations (L, M, H), as described in Section 3. The shaded area shows the $1\,\sigma$ expected errors for the 21 cm-L-M survey described in Section 5. Middle: The 21 cm bias factor extracted from our three cross-spectra approach in the different line-luminosity models. These are compared with that inferred from the 21 cm auto-spectrum (solid gray) and the 21 cm-density cross-spectrum (gray dashed). Bottom: The relative difference between the different bias-factor models. On large scales all inferences agree.

the approach breaks down at the $\sim 10\%$ level at $k \sim 0.3\,\mathrm{Mpc}^{-1}$, though an accuracy of only a few percent is achieved at the largest scales considered here. We sus-

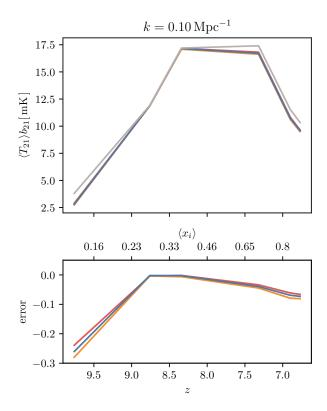


Figure 2. Upper: The inferred 21 cm bias factor as a function of redshift/volume-average ionization fraction at $k=0.1\,\mathrm{Mpc^{-1}}$. The different colored lines show inferences from our three cross-spectra approach in the different line-luminosity models (see Figure 1 and text). The gray line shows the true bias factor measured from the 21 cm- δ cross-spectrum. Lower: The relative error in the three cross-spectra approach. We find better than 5% agreement for most of the EoR with sub-percent accuracy achieved near $\langle x_i \rangle = 0.36$ at z=8.34. At $\langle x_i \rangle \sim 0.15$ the fields decorrelate on large scales and so the approach breaks down (see text).

pect better agreement on even larger scales than probed by our relatively small simulation volume.

In Figure 2 we turn to consider the redshift evolution of the 21 cm bias factor at $k=0.1\,\mathrm{Mpc^{-1}}$. As emphasized earlier, the redshift evolution of the 21 cm bias factor encodes interesting information about how reionization proceeds. The three cross-spectra method generally recovers the overall evolution of the 21 cm bias factor with redshift and volume-averaged ionization fraction quite accurately. This suggests that our technique may help in reconstructing the reionization history of the Universe, or in verifying the results from 21 cm auto-spectrum measurements.

The one exception is near $\langle x_i \rangle \sim 0.15$, where our technique is relatively inaccurate. This occurs because large-scale overdense regions are initially brighter in 21 cm than typical regions in our model and so the 21 cm fields

are intially positively-correlated with the density fluctuations. As reionization begins, the large-scale overdense regions ionize first which causes the correlation coefficient between the 21 cm and density fields to reverse signs. Consequently, there is an intermediate period (near $\langle x_i \rangle \sim 0.15$ in this model) where the two fields are roughly uncorrelated on large scales (Lidz et al. 2008). This causes our method to break down, although we caution that incorporating spin-temperature fluctuations into the modeling may modify this conclusion. Note also that it will be challenging to perform line-intensity mapping observations at very early times before, e.g., sufficient metal enrichment occurs.

While our baseline model assumes the abundant minihalo sinks scenario we have also investigated the fiducial model used in Lidz et al. (2008). Although this latter model has a different ionization history and bias factor evolution, the accuracy of our three cross-spectra method is broadly similar in this case. For example, near the midpoint of reionization in this model $(z = 7.32, \langle x_i \rangle = 0.54)$, the 21 cm bias extraction also reaches sub-percent accuracy.

5. DETECTABILITY

Encouraged by the success of our approach in simulations, we briefly describe the survey specifications required to infer 21 cm bias factors using this technique. Here we consider only rough estimates and defer an in depth treatment of noise power spectra, variance from residual foregrounds, and a full probabilistic, multi-field framework to future work.

We first describe the relevant variance and covariance formulae (for derivations, see e.g. Villaescusa-Navarro et al. 2015):

$$Var[P_{i,j}] = P_{i,j}^2 + P_{i,\text{tot}} P_{j,\text{tot}}$$

$$Cov[P_{i,j}, P_{i,k}] = P_{i,\text{tot}} P_{j,k} + P_{i,j} P_{i,k},$$
(11)

where $P_{i,\text{tot}} = P_i + N_i$ and N_i is the instrumental noise power spectrum of line i. For simplicity, we neglect the shot-noise contribution to each field. We note that Equation 11 is only valid in the Gaussian approximation, but this is suitable for the large scales of interest in our approach.

We can now apply the standard propagation of errors formula to Equation 7 and substitute Equation 11,

yielding:

$$Var[P_{21}] = \left(\frac{P_{21,C \text{ II}}}{P_{21,O \text{ III}}}\right)^{2} \left(P_{21,O \text{ III}}^{2} + P_{21,\text{tot}}P_{O \text{ III,tot}}\right) + \left(\frac{P_{21,O \text{ III}}}{P_{21,C \text{ II}}}\right)^{2} \left(P_{21,C \text{ II}}^{2} + P_{21,\text{tot}}P_{C \text{ II,tot}}\right) + \left(\frac{P_{21,C \text{ II}}P_{21,O \text{ III}}}{P_{C \text{ II,O III}}}\right)^{2} \left(P_{C \text{ II,O III}}^{2} + P_{C \text{ II,tot}}P_{O \text{ III,tot}}\right) + \left(\frac{P_{21,C \text{ II}}P_{21,O \text{ III}}}{P_{C \text{ II,O III}}^{2}}\right)^{2} \left(P_{C \text{ II,O III}} + P_{C \text{ II,O III}} + P_{21,C \text{ II}}P_{21,O \text{ III}}\right) - \frac{P_{21,C \text{ II}}P_{21,O \text{ III}}}{P_{C \text{ II,O III}}^{2}} \left(P_{O \text{ III,tot}}P_{21,C \text{ II}} + P_{21,O \text{ III}}P_{C \text{ II,O III}}\right) - \frac{P_{21,C \text{ II}}P_{21,O \text{ III}}}{P_{C \text{ II,O III}}^{2}} \left(P_{C \text{ II,tot}}P_{21,O \text{ III}} + P_{21,C \text{ II}}P_{C \text{ II,O III}}\right).$$

$$(12)$$

The number of modes in a bin of width δk centered on k is,

$$N_m = \frac{4\pi k^2 \delta k}{V_{\text{fund}}},\tag{13}$$

where V_{fund} is the volume of a fundamental mode. We assume a square survey area and therefore compute,

$$V_{\text{fund}} = \frac{(2\pi)^3}{L_\perp^2 L_\parallel},$$
 (14)

where L_{\perp} is the side length of the survey area and L_{\parallel} is the length of the redshift bin Δz .

We assume a joint survey area of $100\deg^2$ and bin widths of $\delta k = 0.03 \mathrm{Mpc}^{-1}$ and $\Delta z = 0.25$. In order to make a rough estimate, we assume that each experiment reaches sample-variance limited sensitivity at $k = 0.1 \,\mathrm{Mpc}^{-1}$, with $N_i = P_i$ at this wavenumber and adopt a pure, isotropic white-noise power spectrum. In the case of [C II], the required noise depends on the uncertain average specific intensity which determines, in part, the signal strength, P_i . A plausible value is $\langle I_{\rm C\ II} \rangle = 5 \times 10^2 \, \rm Jy/str$ at z = 8.34 (Beane & Lidz 2018). In this case, $N_{\rm C\ II} = 1.6 \times 10^9$, 2.5×10^9 , $3.9 \times 10^9 \, (\mathrm{Jy/str})^2 \, \mathrm{Mpc}^3$ for the L, M, and H models of the [C II] line, respectively at z = 8.34. These noise requirements are comparable to the values forecasted for Stage-II [C II] line-intensity mapping forecasts in Silva et al. (2015a); Lidz & Taylor (2016). We expect broadly similar noise requirements for hypothetical future [O III] surveys but defer detailed forecasts to future work. As we discussed previously (Beane & Lidz 2018). the 21 cm sensitivity requirement assumed here seems plausible considering HERA-350 will image some large

Table 1. The noise power-spectrum for upcoming [C II] surveys at z = 7.4.

survey	A_{survey}	$A_{ m pix}$	$N_{ m C~{\scriptscriptstyle II}}$
	(\deg^2)	(\deg^2)	$((\mathrm{Jy/sr})^2\mathrm{Mpc}^3)$
CCAT-p	2	2.5×10^{-4}	2.66×10^{9}
CONCERTO	1.4	6.7×10^{-5}	2.04×10^{9}
TIME	1.3×0.0084	6.7×10^{-5}	1.04×10^{9}

References—See Chung et al. (2018) for more details.

scale modes (DeBoer et al. 2017) — although the white noise approximation is rather crude and should be refined in future work.

We caution that the strength of the [C II] signal at the redshifts of interest is quite uncertain. A broad range of estimates appear in the current literature, depending on assumptions about: the correlation between [C II] luminosity and SFR at high redshift, the total star-formation rate density (estimates from UV luminosity functions are sensitive to whether and how one extrapolates to faint luminosities beyond current detection limits), and the host-halo masses of [C II] emitters. For example, our model values for $\langle I_{C \text{ II}} \rangle$ are similar to a number of recent forecasts (Dumitru et al. 2018; Silva et al. 2015b), but are more than an order of magnitude larger than some more pessimistic estimates in Silva et al. (2015b); Chung et al. (2018). In any case, at fixed luminosityweighted bias, the required noise scales quadratically with the average specific intensity and so the reader can rescale our results according to their preferred specific intensity model. For instance, in the case of $\langle I_{C \text{ II}} \rangle =$ 20 Jy/sr (Chung et al. 2018), one would require that $N_{C \text{ II}} = 2.6 \times 10^6, \ 4 \times 10^6, \ 6.2 \times 10^6 \ (\text{Jy/sr})^2 \, \text{Mpc}^3 \text{ for}$ the L, M, and H models of the [C II] line, respectively at z = 8.34. On the other hand, a more moderate estimate of $\langle I_{\rm C\ II} \rangle = 100\,{\rm Jy/sr}$ (Silva et al. 2015b; Dumitru et al. 2018), requires $N_{C \text{ II}} = 6.4 \times 10^7$, 1×10^8 , $1.6 \times 10^8 \, (\mathrm{Jy/sr})^2 \, \mathrm{Mpc}^3$ for the L, M, and H models of the [C II] line, respectively at z = 8.34.

With the assumed noise and survey requirements for our fiducial model, we show the resulting error bars in the *Upper* and *Middle* panels of Figure 1 for our particular choice of binning. At least for the hypothetical surveys considered here, the 21 cm bias factor may be recovered with good statistical precision. In other words, if sample-variance limited sensitivity may be reached at $k=0.1\,\mathrm{Mpc}^{-1}$ in each line over a common survey area of $\sim 100\,\mathrm{deg}^2$, then a strong detection appears feasible. Of course we have neglected sample variance contributions

from residual foregrounds among other complications, and so this should be interpreted as a best-case scenario. On the other hand, increasing the common survey area above $100\,\mathrm{deg}^2$, for example, could help shrink the error bars.

While our fiducial [C II] survey is somewhat futuristic. we can also consider the prospects with current, shortly upcoming surveys, specifically CCAT-prime⁷ (Stacey et al. 2018), CONCERTO⁸ (Lagache 2017), and TIME⁹ (Crites et al. 2014). We use the pixel noise values, $\sigma_{\rm pix}t_{\rm pix}^{-1/2}$, for each survey from Chung et al. (2018). We report the noise power spectrum at z = 7.4 (assuming a pure white-noise spectrum) in Table 1. We generically find that $N \sim 2 \times 10^9 \, (\mathrm{Jy/sr})^2 \, \mathrm{Mpc}^3$. If we assume a model with $\langle I_{\rm C~II} \rangle \sim 500\,{\rm Jy/sr}$ then even the firstgeneration surveys reach our requisite noise. However, deeper surveys will be needed in the case of the more pessimistic estimates of $\langle I_{\rm C\ II} \rangle \sim 100$ or $\sim 20\,{\rm Jy/sr.}$ That being said, our fiducial calculations also assume a larger survey area of $100 \deg^2$. At z = 8.34 we find a S/N of 3.3, 2.7, and 2.9 for the L-M, M-H, and H-L models, respectively at $k = 0.1 \,\mathrm{Mpc}^{-1}$ and bin width of $\Delta k = 0.03 \,\mathrm{Mpc}^{-1}$. Since the number of modes scale with the square root of the survey area, we estimate that CCAT-p might be able to recover a S/N of 0.5, 0.4, and 0.4 for the L-M, M-H, and H-L models, respectively at $k = 0.1 \,\mathrm{Mpc}^{-1}$. Including some higher kmodes, even this first-generation survey might be capable of a marginal detection (if [O III] can be surveyed as well), but this is only for our optimistic signal strength model.

Since the strength of the [C II] signal is likely a strong function of redshift, the survey requirements should be less stringent at $z\sim 7$ than the $z\sim 8$ case considered above. The main effect here should be from redshift evolution in the average specific intensity; again, the noise requirements scale with the average intensity squared. The required noise can therefore be adjusted according to one's preferred model for redshift evolution in the signal strength.

6. CONCLUSIONS

We have shown that the amplitude of large-scale 21 cm fluctuations may be inferred from measuring cross-power spectra between the 21 cm fluctuations and each of two separate line-intensity maps, such as [C II] or [O III]. Although it has long been recognized that the cross-power spectrum between two fields is more robust

⁷ http://www.ccatobservatory.org

⁸ https://people.lam.fr/lagache.guilaine/CONCERTO.html

⁹ https://cosmology.caltech.edu/projects/TIME

to foreground contamination than the auto-power spectrum of either field alone, the amplitude of a single cross-power spectrum provides only a product of two bias factors. We found that using a suitable combination of three cross-power spectra (Equations 6 and 7) one can instead infer the 21 cm bias alone to high accuracy.

Quantitatively, in the reionization model we considered, the accuracy reaches percent-level on large scales $(k \sim 0.1 - 0.3 \,\mathrm{Mpc}^{-1})$ during much of the EoR. The inferred bias factor evolution can then be compared to that extracted from the 21 cm auto spectrum. In principle, checking whether the 21 cm auto-power spectrum follows linear-biasing on large scales might itself be a good systematics check. However, linear biasing holds only over a limited span of wavenumbers and early measurements may probe a small dynamic range in spatial scale. Hence we believe that our three cross-spectra approach might play an important role in confirming initial detections. Since our method underestimates $P_{21,21}$ on intermediate scales, it can place informative lower limits (i.e. $\sim 50\%$ of the true value) down to $k \sim 1 \,\mathrm{Mpc}^{-1}$, depending on the stage of reionization. More work is necessary, however, to see if there are some allowed reionization and line-intensity models where our technique actually overestimates $P_{21,21}$.

Although we focused here on the case of 21 cm fluctuations during the EoR, the method has broader applicability. For example, one can also estimate the bias

of the [C II] and [O III] fluctuations by using a similar ratio of cross-spectra. This should help circumvent the line-interloper problem that presents a challenge for such surveys (e.g. Kovetz et al. 2017). Since the ionized bubbles lead to scale-dependent biasing in the 21 cm field on large spatial scales, the 21 cm case is an especially demanding application, and we expect even better performance for [C II], [O III], and related lines.

In order to implement the strategy proposed here, there must be a coordinated effort to probe the same regions on the sky over common redshifts in multiple lines of interest. Ultimately, we envision line-intensity mapping surveys in N different lines, all probing the same cosmological volume. Among other benefits, this will provide N(N-1)/2 measurements of the bias factor in each line using the same basic technique outlined here.

We thank the anonymous referee for providing helpful comments. We thank Matt McQuinn for the simulations used in this analysis. A.B. would like to thank Todd Phillips for helpful discussions. A.B. was supported in part by the Roy & Diana Vagelos Program in the Molecular Life Sciences and the Roy & Diana Vagelos Challenge Award. The work of A.B. and F.V.-N. is supported by the Simons Foundation.

Software: colossus (Diemer 2018), matplotlib (Hunter 2007), numpy (Van Der Walt et al. 2011), and scipy (Jones et al. 2001-).

REFERENCES

Beane, A., & Lidz, A. 2018, ApJ, 867, 26

Bernardi, G., de Bruyn, A. G., Brentjens, M. A., et al. 2009, A&A, 500, 965

Chang, T.-C., Pen, U.-L., Bandura, K., & Peterson, J. B. 2010, Nature, 466, 463

Chung, D. T., Li, T. Y., Viero, M. P., Church, S. E., & Wechsler, R. H. 2017, Astrophys. J., 846, 60

Chung, D. T., Viero, M. P., Church, S. E., & Wechsler, R. H. 2018, arXiv e-prints, arXiv:1812.08135

Cooray, A., et al. 2016, arXiv:1602.05178

Crites, A. T., Bock, J. J., Bradford, C. M., et al. 2014, in Proc. SPIE, Vol. 9153, Millimeter, Submillimeter, and Far-Infrared Detectors and Instrumentation for Astronomy VII, 91531W

Croft, R. A. C., Miralda-Escud, J., Zheng, Z., Blomqvist, M., & Pieri, M. 2018, arXiv:1806.06050

Croft, R. A. C., Miralda-Escudé, J., Zheng, Z., et al. 2016, MNRAS, 457, 3541 Davis, M., Newman, J. A., Faber, S. M., & Phillips, A. C. 2001, in Deep Fields, ed. S. Cristiani, A. Renzini, & R. E. Williams, 241

DeBoer, D. R., et al. 2017, Publ. Astron. Soc. Pac., 129, 045001

Diemer, B. 2018, ApJS, 239, 35

Dillon, J. S., et al. 2014, Phys. Rev., D89, 023002

Doré, O., Werner, M. W., Ashby, M., et al. 2016, ArXiv e-prints, arXiv:1606.07039

Dumitru, S., Kulkarni, G., Lagache, G., & Haehnelt, M. G. 2018, arXiv e-prints, arXiv:1802.04804

Ewall-Wice, A., Dillon, J. S., Liu, A., & Hewitt, J. 2017, Mon. Not. Roy. Astron. Soc., 470, 1849

Furlanetto, S., & Lidz, A. 2007, Astrophys. J., 660, 1030

Gong, Y., Cooray, A., Silva, M. B., Santos, M. G., & Lubin, P. 2011, ApJL, 728, L46

Hoffmann, K., Mao, Y., Xu, J., Mo, H., & Wandelt, B. D. 2018, arXiv:1802.02578

- Hunter, J. D. 2007, Computing In Science & Engineering, 9, 90
- Jones, E., Oliphant, T., Peterson, P., et al. 2001–, SciPy: Open source scientific tools for Python, , . http://www.scipy.org/
- Keating, G. K., Marrone, D. P., Bower, G. C., et al. 2016, Astrophys. J., 830, 34
- Kovetz, E. D., Viero, M. P., Lidz, A., et al. 2017, ArXiv e-prints, arXiv:1709.09066
- Lagache, G. 2017, IAU Symp., 333, 228
- Lidz, A., Furlanetto, S. R., Oh, S. P., et al. 2011, ApJ, 741, 70
- Lidz, A., & Taylor, J. 2016, ApJ, 825, 143
- Lidz, A., Zahn, O., Furlanetto, S., et al. 2009, Astrophys. J., 690, 252
- Lidz, A., Zahn, O., McQuinn, M., Zaldarriaga, M., & Hernquist, L. 2008, ApJ, 680, 962
- Liu, A., & Tegmark, M. 2012, MNRAS, 419, 3491
- Mao, Y., Shapiro, P. R., Mellema, G., et al. 2012, MNRAS, 422, 926
- $\operatorname{McQuinn},\,\operatorname{M.},\,\&$ D'Aloisio, A. 2018, JCAP, 1810, 016
- McQuinn, M., Hernquist, L., Zaldarriaga, M., & Dutta, S. 2007, Mon. Not. Roy. Astron. Soc., 381, 75
- McQuinn, M., Lidz, A., Zahn, O., et al. 2007, MNRAS, 377, 1043
- Mesinger, A., Furlanetto, S., & Cen, R. 2011, MNRAS, 411, 955
- Moore, D. F., Aguirre, J. E., Parsons, A. R., Jacobs, D. C., & Pober, J. C. 2013, ApJ, 769, 154
- Moriwaki, K., Yoshida, N., Shimizu, I., et al. 2018, MNRAS, 481, L84
- Park, J., Mesinger, A., Greig, B., & Gillet, N. 2018, ArXiv e-prints, arXiv:1809.08995

- Planck Collaboration, Aghanim, N., Akrami, Y., et al. 2018, ArXiv e-prints, arXiv:1807.06209
- Pober, J. C., Parsons, A. R., Aguirre, J. E., et al. 2013, ApJL, 768, L36
- Pober, J. C., Hazelton, B. J., Beardsley, A. P., et al. 2016, ApJ, 819, 8
- Pullen, A. R., Serra, P., Chang, T.-C., Doré, O., & Ho, S. 2018, MNRAS, 478, 1911
- Righi, M., Hernandez-Monteagudo, C., & Sunyaev, R. 2008, Astron. Astrophys., 489, 489
- Serra, P., Dor, O., & Lagache, G. 2016, Astrophys. J., 833, 153
- Silva, M., Santos, M. G., Cooray, A., & Gong, Y. 2015a, ApJ, 806, 209
- —. 2015b, ApJ, 806, 209
- Springel, V. 2005, Mon. Not. Roy. Astron. Soc., 364, 1105
- Stacey, G. J., Aravena, M., Basu, K., et al. 2018, in Society of Photo-Optical Instrumentation Engineers (SPIE) Conference Series, Vol. 10700, Ground-based and Airborne Telescopes VII, 107001M
- Suginohara, M., Suginohara, T., & Spergel, D. N. 1999, Astrophys. J., 512, 547
- Thyagarajan, N., Jacobs, D. C., Bowman, J. D., et al. 2015, ApJ, 804, 14
- Van Der Walt, S., Colbert, S. C., & Varoquaux, G. 2011, ArXiv e-prints, arXiv:1102.1523
- Vavagiakis, E. M., et al. 2018
- Villaescusa-Navarro, F., Viel, M., Alonso, D., et al. 2015, JCAP, 3, 034
- Visbal, E., & Loeb, A. 2010, JCAP, 11, 016
- Zaldarriaga, M., Furlanetto, S. R., & Hernquist, L. 2004, Astrophys. J., 608, 622